

High angular resolution Sunyaev-Zel'dovich observations of MACS J1423.8+2404 with NIKA: multi-wavelength analysis

R. Adam^{1,2*}, B. Comis¹, I. Bartalucci³, A. Adane⁴, P. Ade⁵, P. André³, M. Arnaud³,
A. Beelen⁶, B. Belier⁷, A. Benoît⁸, A. Bideaud⁵, N. Billot⁹, O. Bourrion¹, M. Calvo⁸,
A. Catalano¹, G. Coiffard⁴, A. D'Addabbo^{8,10}, F.-X. Désert¹¹, S. Doyle⁵, J. Goupy⁸,
B. Hasnoun⁶, I. Hermelo⁹, C. Kramer⁹, G. Lagache¹², S. Leclercq⁴, J.-F. Macías-Pérez¹,
J. Martino⁶, P. Mauskopf^{5,13}, F. Mayet¹, A. Monfardini⁸, F. Pajot⁶, E. Pascale⁵,
L. Perotto¹, E. Pointecouteau^{14,15}, N. Ponthieu¹¹, G.W. Pratt³, V. Revéret³, A. Ritacco¹,
L. Rodriguez³, G. Savini¹⁶, K. Schuster⁴, A. Sievers⁹, S. Triqueneaux⁸, C. Tucker⁵, and
R. Zylka⁴

¹ Laboratoire de Physique Subatomique et de Cosmologie, Université Grenoble-Alpes, CNRS/IN2P3, 53, rue des Martyrs, Grenoble, France

² Laboratoire Lagrange, Université Côte d'Azur, Observatoire de la Côte d'Azur, CNRS, Blvd de l'Observatoire, CS 34229, 06304 Nice cedex 4, France

³ Laboratoire AIM, CEA/IRFU, CNRS/INSU, Université Paris Diderot, CEA-Saclay, 91191 Gif-Sur-Yvette, France

⁴ Institut de RadioAstronomie Millimétrique (IRAM), Grenoble, France

⁵ Astronomy Instrumentation Group, University of Cardiff, UK

⁶ Institut d'Astrophysique Spatiale (IAS), CNRS and Université Paris Sud, Orsay, France

⁷ Institut d'Electronique Fondamentale (IEF), Université Paris Sud, Orsay, France

⁸ Institut Néel, CNRS and Université de Grenoble, France

⁹ Institut de RadioAstronomie Millimétrique (IRAM), Granada, Spain

¹⁰ Dipartimento di Fisica, Sapienza Università di Roma, Piazzale Aldo Moro 5, I-00185 Roma, Italy

¹¹ Institut de Planétologie et d'Astrophysique de Grenoble (IPAG), CNRS and Université de Grenoble, France

¹² Aix Marseille Université, CNRS, LAM (Laboratoire d'Astrophysique de Marseille) UMR 7326, 13388, Marseille, France

¹³ School of Earth and Space Exploration and Department of Physics, Arizona State University, Tempe, AZ 85287

¹⁴ Université de Toulouse, UPS-OMP, Institut de Recherche en Astrophysique et Planétologie (IRAP), Toulouse, France

¹⁵ CNRS, IRAP, 9 Av. colonel Roche, BP 44346, F-31028 Toulouse cedex 4, France

¹⁶ University College London, Department of Physics and Astronomy, Gower Street, London WC1E 6BT, UK

Abstract

NIKA, the prototype of the NIKA2 camera, is a dual-band instrument operating at the IRAM 30-meter telescope that can observe the sky simultaneously at 150 and 260 GHz. One of the main goals of NIKA (and NIKA2) is to measure the pressure distribution in galaxy clusters at high angular resolution using the thermal Sunyaev-Zel'dovich (tSZ) effect. Such observations have already proved to be an excellent probe of cluster pressure distributions even at intermediate and high redshifts. However, an important fraction of clusters host sub-millimeter and/or radio point sources that can significantly affect the reconstructed signal. Here we report < 20 arcsec angular resolution observations at 150 and 260 GHz of the cluster MACS J1423.8+2404, which hosts both radio and sub-millimeter point sources. We examine the morphological distribution of the tSZ signal and compare it to other datasets. The NIKA data are combined with Herschel satellite data to study the spectral energy distribution (SED) of the sub-millimeter point source contaminants. We then perform a joint reconstruction of the intracluster medium (ICM) electronic pressure and density by combining NIKA, Planck, XMM-Newton and Chandra data, focussing on the impact of the radio and sub-millimeter sources on the reconstructed pressure profile. We find that the large-scale pressure distribution is unaffected by the point sources due to the resolved nature of the NIKA observations. The reconstructed pressure in the inner region is slightly higher when the contribution of point sources are removed. We show that it is not possible to set strong constraints on the central pressure distribution without removing accurately these contaminants. The comparison with X-ray only data shows good agreement for the pressure, temperature and entropy profiles, all indicating that MACS J1423.8+2404 is a dynamically relaxed cool core system. The present observations illustrate the possibility of measuring these quantities with a relatively small integration time, even at high redshift and without X-ray spectroscopy. This work is part of a pilot study aiming at optimizing tSZ observations with the future NIKA2 camera.

Key words. Techniques: high angular resolution – Galaxies: clusters: individual: MACS J1423.8+2404; intracluster medium

1. Introduction

In the standard scenario of structure formation, clusters of galaxies form by the hierarchical merging of smaller groups and the accretion of surrounding material. They are sensitive to both the matter content of the Universe and its dynamics because they form throughout its expansion history. Their formation process is well understood and clusters have been used to place constraints on cosmological parameters (e.g. [Planck Collaboration et al. 2013b](#)). However, the complex baryonic physics occurring during cluster formation, such as feedback from active galactic nuclei (AGN), or non-thermal processes occurring during mergers or in the presence of ICM turbulence or coherent motion, is still unclear (see for example [Borgani & Kravtsov 2011](#)). This leads to scatter and biases in the observable–mass scaling relations needed to compare to theory, limiting the use of clusters as cosmological probes.

The thermal Sunyaev-Zel'dovich effect (tSZ, [Sunyaev & Zel'dovich 1972, 1980](#)) is produced by the inverse Compton interaction of cosmic microwave background (CMB) photons with the energetic electrons in the intracluster medium (ICM). It leads to a spectral distortion of the CMB observable at millimeter and sub-millimeter wavelengths that is directly proportional to the line-of-sight integral of the electronic pressure distribution in the ICM. The integrated tSZ flux is related

* Corresponding author: Rémi Adam, remi.adam@oca.fr

Please give a shorter version with: \authorrunning and/or \titilerunning prior to \maketitle

to the overall thermal energy of the cluster and is therefore expected to provide a low scatter mass proxy with a small dependence on the dynamical state of the cluster or the exact gas physics (e.g. da Silva et al. 2004; Motl et al. 2005; Nagai 2006). Furthermore, resolved tSZ observations are very sensitive to the overpressure caused by mergers and have proved to be very efficient for probing cluster astrophysics (see for example results by Pointecouteau et al. 1999; Komatsu et al. 2001; Korngut et al. 2011; Adam et al. 2014; Young et al. 2014; Adam et al. 2015; Mroczkowski et al. 2015). This is particularly true at high redshifts since, unlike other probes, the tSZ signal does not suffer from cosmological dimming, and is only limited by the sensitivity and angular resolution of the observations. Detailed reviews of the tSZ effect can be found in Birkinshaw (1999); Carlstrom et al. (2002); Kitayama (2014).

During the past few years, tremendous achievements have been made in the tSZ community, with the production of catalogues of more than 1 000 objects by Planck (Planck Collaboration et al. 2013a), the Atacama Cosmology Telescope (ACT, Hasselfield et al. 2013) and the South Pole Telescope (SPT, Reichardt et al. 2013; Bleem et al. 2014), at > 1 arcmin angular resolution. X-ray observations have shown that, when scaled to a characteristic radius, the cluster pressure profile shows a low dispersion (Arnaud et al. 2010). This profile has now been well measured at intermediate scales in the nearby Universe with tSZ observations (Planck Collaboration et al. 2013c; Sayers et al. 2013a) but remains largely unexplored at high redshift and in the cluster cores, because of the lack of high-angular resolution observations. Its investigation is nonetheless necessary for a better use of the available tSZ cluster samples when relating the tSZ signal to cluster mass.

In the coming years, the New IRAM Kids Array 2 (NIKA2 Monfardini et al. 2014) will be used to map the tSZ signal from clusters of galaxies with an 18 arcsec angular resolution at 150 GHz. The NIKA2 camera¹ is the next generation continuum instrument for the IRAM (Institut de Radio Astronomie Millimétrique) 30-meter telescope near Granada, Spain. It consists of a dual-band camera made of about 5000 kinetic inductance detectors sampling a 6.5 arcmin field of view, observing the sky at 150 and 260 GHz. NIKA2 will be installed during the autumn 2015 and commissioned in the following winter.

In the context of tSZ observations, one of the main challenges NIKA2 will have to face will be the removal of the contamination from point sources, as needed for example in the case of Bolocam observations (Sayers et al. 2013b). Indeed, galaxy clusters contain galaxies that can host radio sources or a significant amount of dust. In addition, clusters at intermediate redshift provide optimal lenses, which can magnify sub-millimeter background galaxies (see e.g. Adam et al. 2015). Foreground galaxies can also be located in projection near the cluster under study. In tSZ observations, these objects appear as point-like contaminating sources. NIKA is the prototype of NIKA2 (see Monfardini et al. 2010; Bourrion et al. 2011, 2012; Monfardini et al. 2011; Calvo et al. 2013; Catalano et al. 2014 for more details on the NIKA camera). It has already been used to image the tSZ effect towards the galaxy clusters RX J1347.5-1145 and CL J1226.9+3332, (see Adam et al. 2014, 2015). In the present paper we discuss observations of the intermediate redshift cluster MACS J1423.8+2404 at $z = 0.545$, which contains both radio and sub-millimeter galaxies and which we have used as a test case to investigate the impact of such contaminating objects on the reconstruction of the pressure of clusters observed with NIKA2.

¹ <http://ipag.osug.fr/nika2/Welcome.html>

MACS J1423.8+2404 is a massive cluster from the MACS catalog (Massive Cluster Survey, Ebeling et al. 2001), for which a wealth of multi-wavelength data have been obtained. Schmidt & Allen (2007), in a study of relaxed clusters with Chandra, reported a virial mass $M_{\text{vir}} = 4.52^{+0.79}_{-0.64} \times 10^{14} M_{\odot}$, indicating that it indeed is a massive object. The cluster was observed by the BIMA interferometer (LaRoque et al. 2003), and by the Sunyaev-Zel’dovich Array (SZA) (Bonamente et al. 2012), as part of a sample used to constrain the cluster pressure profile. The large scale structure of MACS J1423.8+2404 was investigated using its red sequence galaxy density distribution (Kartaltepe et al. 2008), showing a very relaxed morphology. Guennou et al. (2014) have studied the structure of the cluster using Chandra X-ray data, as part of the DAFT/FADA survey. They observed a strong X-ray emission, slightly elongated, and only low significance substructures were found. The morphology of the cluster was also studied from a detailed gravitational lensing/optical analysis by Limousin et al. (2010), who noticed that MACS J1423.8+2404 is nearly fully virialized, elongated, and shows very little substructure (see also the strong lensing results by Zitrin et al. (2011), as part of a sample of 12 MACS clusters). The temperature profile obtained by Morandi et al. (2010) using Chandra data shows a typical cool core form, with a low central temperature (~ 3 keV) and a peak at ~ 7 keV at about 300 kpc away from the center. The brightest cluster galaxy (BCG) hosts a central AGN that is visible as a point source in radio observations (Condon et al. 1998; LaRoque et al. 2003; Coble et al. 2007; Bonamente et al. 2012). This AGN is responsible for the presence of two cavities detected in the Chandra X-ray image (Hlavacek-Larrondo et al. 2012). Another radio source is located at about 1.5 arcmin south-west with respect to the X-ray peak. Cluster members, foreground, background (including lensed sources) sub-millimeter galaxies are detected by Herschel, as observed during the Herschel Lensing Survey (HLS, Egami et al. 2010; Rawle et al. 2012).

This paper is organized as follows. The observations performed at the IRAM 30-meter telescope are briefly presented in Sect. 2. In Sect. 3, we discuss the processing of radio and sub-millimeter point sources and their impact on the radial tSZ flux density profile. The data reduction of the XMM-Newton and Chandra X-ray observations is presented in Sect. 4. We compare the NIKA observations to other multi-wavelength datasets in Sect. 5. In Sect. 6, we reconstruct the radial pressure distribution of MACS J1423.8+2404 and explore the impact of the presence of the point sources. The pressure profile is combined with the electronic density of X-ray data to derive the thermodynamic distribution of the ICM. Conclusions and perspectives for NIKA2 are provided in Sect. 7. Throughout this paper we assume a flat Λ CDM cosmology according to the latest Planck results (Planck Collaboration 2015) with $H_0 = 67.8 \text{ km s}^{-1} \text{ Mpc}^{-1}$, $\Omega_M = 0.308$, and $\Omega_{\Lambda} = 0.692$.

2. Observation at the IRAM 30-meter telescope with NIKA

2.1. The thermal Sunyaev-Zel’dovich effect

The tSZ effect (Sunyaev & Zel’dovich 1972, 1980) results in a distortion of the CMB black-body spectrum relative to the primary CMB intensity, I_0 , (e.g. Birkinshaw 1999)

$$\frac{\Delta I_{\text{tSZ}}}{I_0} = y f(\nu, T_e). \quad (1)$$

The function $f(\nu, T_e)$ gives the characteristic frequency dependence of the spectrum. The small dependance on the electronic temperature, T_e , arises from relativistic corrections for which we use

Please give a shorter version with: \authorrunning and/or \titilerunning prior to \maketitle

the results of [Itoh et al. \(1998\)](#) in this paper. The Compton parameter, y , gives the amplitude of the distortion and is related to the line of sight integral of the electronic pressure, P_e , as

$$y = \frac{\sigma_T}{m_e c^2} \int P_e dl. \quad (2)$$

The parameter σ_T is the Thomson cross section, m_e is the electron rest mass, and c the speed of light. The total integrated tSZ flux, Y_{tot} , is then given by the aperture photometry performed on the Compton parameter map.

In the NIKA bands, the tSZ signal is expected to be faint ($y \sim 10^{-4}$ for typical massive clusters) and diffuse. It is negative at 150 GHz, and positive at 260 GHz.

2.2. Observing conditions, scanning strategy, calibration and data reduction

MACS J1423.8+2404 was observed during the first NIKA open pool in February 2014. We collected 1.47 hours of on-target data. The atmospheric conditions were stable and the mean opacity was measured to be 0.14 and 0.15, at the source location, at 150 and 260 GHz, respectively, as detailed in [Catalano et al. \(2014\)](#). The mean elevation of the source was 30.8 degrees.

The scanning strategy adopted was the same as that used for CL J1226.9+3332, detailed in [Adam et al. \(2015\)](#). Briefly, each scan consisted 19 subscans of 6 arcmin length separated by 10 arcsec steps made alternately at constant azimuth and constant elevation (relative to the map center). The pointing center was chosen to be at (R.A., Dec. 2000) = (14:23:47.8, +24:04:40.0) based on the ACCEPT catalog ([Cavagnolo et al. 2009](#)).

The detailed calibration procedure can be found in [Adam et al. \(2015\)](#) and we only summarize the main results here. Uranus was used as the primary calibrator. The Gaussian beam FWHM was measured to be 18.2 and 12.0 arcsec at 150 and 260 GHz respectively. The nearby quasar 1354+195 was used to correct the pointing, for which the error is estimated to be less than 3 arcsec. The overall calibration uncertainty was estimated to be 7% at 150 GHz and 12% at 260 GHz. The NIKA bandpasses were used to convert the flux surface brightness to Compton parameter. We obtained -10.9 ± 0.8 and 3.5 ± 0.5 Jy/beam per unit of Compton parameter at 150 and 260 GHz, respectively. The effective number of detectors was 117 at 150 GHz and 136 at 260 GHz, corresponding to an instantaneous field of view of 1.9 and 1.8 arcmin respectively.

The removal of the atmospheric and electronic correlated noise, consisting of the subtraction of the correlated signal in the timelines across the detector arrays, was performed as in [Adam et al. \(2015\)](#). The resulting signal filtering was estimated using simulations. The observed transfer function was flat and close to unity at scales that are smaller than the field of view, and vanishes smoothly at larger angular scales (see [Adam et al. 2015](#)).

2.3. Raw NIKA observations

The NIKA maps that we obtained are presented in Fig. 1. The 150 GHz map reveals a negative decrement, as expected from the tSZ effect at this frequency, with a maximum significance of 4.5σ . The morphology of the signal has a ring-like shape, as a consequence of the contamination by the radio point source at the cluster center, which fills in the tSZ signal. The 260 GHz map does not show any significant tSZ signal. At this frequency, extrapolating from the 150 GHz map, we expect a peak of ~ 1 mJy/beam, which is below the level of the noise standard deviation. We

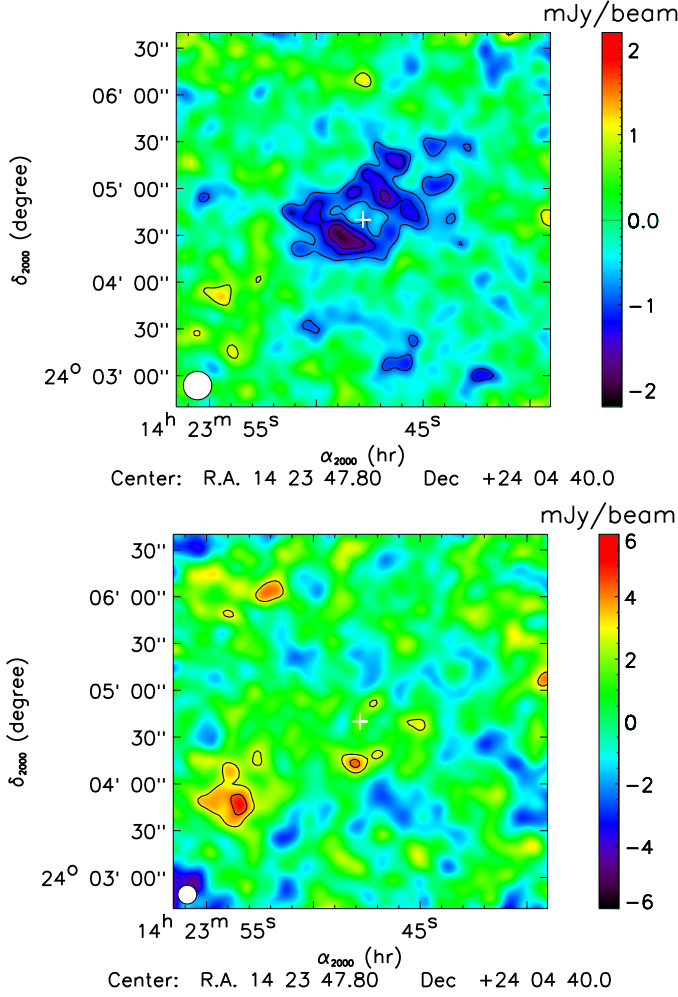


Figure 1. NIKA maps at 150 GHz (left) and 260 GHz (right) in units of surface brightness. The significance is given by the black contours starting at $\pm 2 \sigma$ with 1σ spacing. The maps are smoothed with an extra 10 arcsec Gaussian filter for display purposes and the effective beam FWHM are represented as a white circle in the bottom left corner. The white crosses indicate the X-ray center.

observe a 3σ positive peak around (R.A., Dec.) = (14:23:53, +24:03:45) corresponding to a 2σ positive peak in the 150 GHz map, due to the presence of a sub-millimeter source. Another peak is also seen around (R.A., Dec.) = (+14:23:48, +24:04:15). The radio and sub-millimeter point source contamination will be discussed in detail in Sect. 3.

The significance of the NIKA maps was calculated using Monte Carlo realizations. First, a noise map was obtained from the half difference of two equivalent subsets. After having normalized the noise map by the integration time per pixel, the noise spectral distribution was computed using the POKER software (Ponthieu et al. 2011), which properly accounts for incomplete sky coverage due to the scanning around the cluster. The noise power spectrum was modeled as a function of angular scale k , as $P_{\text{noise}}(k) = A_{\text{white}} + A_{\text{cor}}(k_0) \left(\frac{k}{k_0}\right)^\beta$. The parameter A_{white} represents the intrinsic detector noise and A_{cor} and β give the amplitude and the slope of the residual detector–detector atmospheric correlations in the map. This model was used to generate Monte-Carlo noise map realizations, n_i , accounting for the integration time per pixel. The noise realizations were smoothed by the same 10 arcsec Gaussian filter used to display the cluster, and the standard deviation across the Monte-

Carlo realizations allowed us to compute the root mean square map and therefore the signal to noise contours shown in Fig. 1. The full noise covariance matrix was also computed as the mean of the noise covariance over all the realizations, $C = \frac{1}{N_{\text{MC}}} \sum_{i=1}^{N_{\text{MC}}} n_i n_i^T$ and it is used in the analysis as described in Sect. 6.

3. Radio and sub-millimeter point sources

3.1. Radio point sources

VLA (Very Large Array) data at 4.8 GHz were used by LaRoque et al. (2003) to detect radio sources towards MACS J1423.8+2404. Two sources were detected within the NIKA field and we used the coordinates obtained by LaRoque et al. (2003) as a reference (see Sect. 5 and Fig. 4). The first source, hereafter RS1, is located within the central BCG, near the X-ray center. The second, hereafter RS2, is located at about 1.5 arcmin towards the south-west. The flux of RS1 was measured at various radio wavelengths between 1.4 GHz and 30 GHz while the flux of RS2 has only been measured at 1.4 and 4.8 GHz. We list in Table 1 the fluxes measured for both sources and the corresponding references.

Table 1. Location and flux of the radio sources observed in the 4×4 arcmin² field around MACS J1423.8+2404.

Source	Identifier	Position	1.4 GHz	4.8 GHz	28.5 GHz	30 GHz
		[mJy]	[mJy]	[mJy]	[mJy]	
RS1	NVSS J142347+240439	14:23:47.78 +24:04:42.8 ^(a)	$8.0 \pm 1.1^{(b)}$	$4.40 \pm 0.03^{(a)}$	$1.49 \pm 0.12^{(c)}$	$2.0 \pm 0.2^{(d)}$
RS2	NVSS J142345+240340	14:23:45.07 +24:03:42.7 ^(a)	$7.2 \pm 0.5^{(b)}$	$2.72 \pm 0.03^{(a)}$	–	–

Notes. ^(a) VLA, LaRoque et al. (2003). ^(b) NVSS, Condon et al. (1998). ^(c) OVRO/BIMA, Coble et al. (2007). ^(d) SZA, Bonamente et al. (2012).

To estimate the expected flux of each source in the NIKA bands, we modeled their SED by $F_\nu = F_{1 \text{ GHz}} \left(\frac{\nu}{1 \text{ GHz}} \right)^{\alpha_{\text{radio}}}$. The fluxes reported in Table 1 were used to fit the amplitude of the SED, $F_{1 \text{ GHz}}$, and its slope, α_{radio} . The best-fit parameters are reported in Table 2 for both sources. We then simulated mock SEDs by sampling the parameters within their error bars and accounting for the covariance between them. Each mock SED was then integrated within the NIKA bandpasses to predict the expected flux at 150 and 260 GHz. The histogram of all the realizations was fitted with a Gaussian function to give the expected fluxes and uncertainties, which are listed for both sources and both NIKA frequencies in Table 2. The values of the spectral index α_{radio} we obtain are typical for radio sources (see for example Witzel et al. 1979).

3.2. Sub-millimeter point sources

We make use of the Herschel SPIRE (Griffin et al. 2010) and PACS (Poglitsch et al. 2010) data obtained during the Herschel Lensing Survey (HLS, Egami et al. 2010; Rawle et al. 2012)² to identify sub-millimeter point sources and compute their expected spectral energy distribution (SED)

² Obs-IDs 1342188159, 1342188215 and 1342188216.

Please give a shorter version with: \authorrunning and/or \titilerunning prior to \maketitle

Table 2. Best-fit parameters and extrapolation of the fluxes in the NIKA bands of the radio sources in the 4×4 arcmin² field around MACS J1423.8+2404. The degeneracy between the slope α_{radio} and the amplitude $F_{1 \text{ GHz}}$ has been accounted for to extrapolate the flux in the NIKA bands. See text for details.

Source	R.A. offset [arcsec]	Dec. offset (arcsec) [arcsec]	$F_{1 \text{ GHz}}$ [mJy]	α_{radio}	150 GHz [mJy]	260 GHz [mJy]
RS1	0.3	2.6	10.39 ± 0.30	-0.548 ± 0.001	0.68 ± 0.08	0.54 ± 0.07
RS2	41.0	-57.3	9.39 ± 0.69	-0.790 ± 0.003	0.18 ± 0.04	0.13 ± 0.03

Table 3. Positions and fluxes of the 17 sub-millimeter sources identified in the 4×4 arcmin² field around MACS J1423.8+2404, measured by fitting Gaussian models to the maps at each wavelength as described in Sect. 3.2. The final two columns correspond to the NIKA bands.

Source	250 μm source position	100 μm [mJy]	160 μm [mJy]	250 μm [mJy]	350 μm [mJy]	500 μm [mJy]	1.15 mm [mJy]	2.05 mm [mJy]
SMG01	14:23:52.31 +24:05:04.9	20.8 ± 1.1	35.1 ± 3.2	52.3 ± 7.7	30.4 ± 8.1	11.6 ± 7.4	0.6 ± 3.2	1.4 ± 0.9
SMG02	14:23:48.16 +24:04:20.0	12.4 ± 1.4	21.0 ± 3.1	35.8 ± 9.8	24.1 ± 7.4	16.3 ± 7.2	4.8 ± 2.9	**
SMG03	14:23:53.50 +24:06:05.1	10.7 ± 1.2	17.0 ± 2.9	34.7 ± 11.3	23.7 ± 7.9	8.2 ± 7.1	3.4 ± 3.8	0.5 ± 1.1
SMG04	14:23:42.42 +24:04:38.8	11.5 ± 1.4	17.7 ± 3.0	29.1 ± 10.8	21.3 ± 8.0	4.4 ± 7.5	2.6 ± 3.2	0.4 ± 0.9
SMG05	14:23:47.58 +24:04:48.7	6.1 ± 1.3	9.4 ± 2.8	25.6 ± 8.4	18.3 ± 7.6	14.3 ± 7.5	3.1 ± 2.9	**
SMG06	14:23:53.32 +24:03:48.5	2.9 ± 1.4	8.5 ± 3.1	20.6 ± 9.6	14.9 ± 8.0	1.8 ± 7.7	8.2 ± 3.4	1.0 ± 0.9
SMG07	14:23:45.04 +24:05:48.9	3.4 ± 1.3	10.2 ± 3.0	20.1 ± 9.2	14.0 ± 8.0	7.3 ± 8.0	1.3 ± 3.4	1.0 ± 0.9
SMG08	14:23:49.16 +24:02:46.1	-1.0 ± 1.5	5.4 ± 3.2	19.9 ± 8.8	24.0 ± 7.8	11.2 ± 7.8	3.5 ± 3.8	0.9 ± 1.0
SMG09	14:23:43.27 +24:02:50.2	2.4 ± 1.3	5.8 ± 3.3	12.6 ± 8.6	13.8 ± 7.7	19.4 ± 7.8	2.5 ± 4.1	-0.1 ± 1.1
SMG10	14:23:44.55 +24:03:18.4	-1.5 ± 1.2	4.4 ± 3.3	11.1 ± 8.2	19.0 ± 7.7	19.7 ± 7.8	4.3 ± 3.4	-0.2 ± 0.9
SMG11	14:23:54.14 +24:05:32.2	7.3 ± 1.3	11.6 ± 2.9	11.0 ± 9.1	3.5 ± 7.5	5.9 ± 7.8	-1.6 ± 3.7	0.3 ± 1.0
SMG12	14:23:43.41 +24:03:50.6	5.4 ± 1.3	9.1 ± 3.2	7.3 ± 10.0	-1.9 ± 7.6	-6.9 ± 7.4	2.3 ± 3.4	0.4 ± 0.9
SMG13	14:23:50.13 +24:06:17.4	11.7 ± 1.3	8.9 ± 3.1	6.4 ± 7.5	-2.4 ± 8.0	-10.5 ± 7.7	-4.2 ± 3.7	0.9 ± 1.0
SMG14	14:23:47.36 +24:05:49.6	3.9 ± 1.3	5.5 ± 2.9	7.9 ± 8.6	10.9 ± 7.8	4.7 ± 7.4	0.3 ± 3.2	-0.2 ± 0.9
SMG15	14:23:40.95 +24:05:08.7	2.4 ± 1.3	3.1 ± 3.3	6.6 ± 9.1	6.8 ± 8.2	8.2 ± 7.4	-1.2 ± 3.5	0.0 ± 0.9
SMG16*	14:23:53.69 +24:04:12.6	6.2 ± 1.4	7.3 ± 3.4	18.0 ± 10.5	-4.0 ± 7.7	-3.5 ± 7.5	3.4 ± 3.3	0.6 ± 0.9
SMG17*	14:23:51.72 +24:05:48.8	4.7 ± 1.3	4.3 ± 3.4	-14.6 ± 9.7	-6.2 ± 7.7	-7.4 ± 7.4	-2.2 ± 3.4	-0.1 ± 0.9

Notes. * Sources for which the position is estimated based on the 100 μm PACS channel. ** Fluxes which are not available due to the tSZ contamination.

as seen by NIKA, as described below. The Herschel data complement those from NIKA, both in terms of wavelength 500, 350, 250, 160 and 100 μm , and angular resolution, FWHM = 35.2, 23.9, 17.6, 9.9, 6.1 arcsec, respectively.

The PACS maps were produced using the maximum likelihood map maker MADmap (Cantalupo et al. 2010), provided as a PACS Photometer Level 2.5 Product. We used the Herschel Source List Product, generated using the software SUSSEXtractor (Savage & Oliver 2007), that contains the location and flux of the sources found around MACS J1424.8+2404. By using all the Herschel frequency bands, we found a total of 17 sub-millimeter sources in the 4×4 arcmin² around the cluster, two of which correspond to the excesses seen in the NIKA 260 GHz map. The

250 μm channel is the most complete, with 15 sources, and we used it as a baseline to define the source positions and labels; the corresponding sources in the other channels were identified on the basis of their positions with respect to those in the 250 μm channel. Two sources peaking at high frequency were not present in the 250 μm catalog and we relied on the 100 μm channel for their properties. Due to the relatively low resolution at 500 and 350 μm , a few sources are confused with their neighbors, and in general, not all the sources are identifiable in all the frequency bands in the catalog. To obtain the fluxes of all sources in all bands, we fit the amplitude of a Gaussian function to each map, with position fixed at the source reference location and FWHM fixed to that of the respective Herschel channels. A local background was also fit. In order to account for the confusion in the flux uncertainties, we fit the same Gaussian function at random positions, where the noise is homogeneous, and use the dispersion as the uncertainty. We checked that the sources present in the catalog have compatible fluxes with respect to those we recovered. The positions and fluxes for all the sources are listed in Table 3.

Similarly, the fluxes of the sub-millimeter sources in the NIKA field were obtained by fitting the amplitude of a Gaussian model, using the NIKA FWHM at the source positions expected from Herschel data. These were then corrected them for the filtering induced by the data reduction (~ 15 percent for point sources). Uncertainties were obtained from the standard deviation of the amplitudes recovered using Gaussian fits performed on the Monte-Carlo noise map realizations. The fluxes obtained and their uncertainties are summarized together with the Herschel data in columns Table 3. By stacking the flux of all the sources, assuming that they are independent, we obtained an average flux of 1.96 ± 0.82 mJy at 260 GHz (1.15 mm) and 0.46 ± 0.25 mJy at 150 GHz (2.05 mm), corresponding to a mean detection of 2.4 and 1.9 σ , respectively. If we exclude the two sources directly detected at the map level, the detection reduces to 1.59 ± 0.89 mJy at 260 GHz (1.8 σ) and 0.45 ± 0.25 mJy (1.8 σ) at 150 GHz.

Only SMG02 and SMG06 are directly detected in the NIKA maps. To better constrain the fluxes in the NIKA bands, we modeled the SED with a modified black-body spectrum, $F_\nu = A_0 \left(\frac{\nu}{\nu_0}\right)^{\beta_{\text{dust}}} B_\nu(T_{\text{dust}})$, where A_0 is a normalization, ν_0 a reference frequency, β_{dust} the dust spectral index and T_{dust} the dust temperature. We noticed a flux excess at 100 μm for most of the sources with respect to the best-fit SED derived from all the other channels, which we attribute to the modified black-body spectrum being too simplistic a description of the data at high frequency. We therefore excluded this frequency for constraining the SED in the following. Since we aim to subtract the sources at 150 GHz, we also excluded the NIKA measurement at this frequency and only checked that predicted and measured fluxes are consistent. For the SMG02 and SMG05 sources, the 150 GHz data were not extracted because of strong contamination by the local tSZ signal.

We performed a Markov Chain Monte Carlo (MCMC) analysis to fit simultaneously for β_{dust} and T_{dust} . This approach allows us to sample the corresponding parameter space and to automatically marginalize over A_0 , which is highly degenerate with the two other parameters. The Metropolis-Hasting algorithm was used to sample the parameter space. Each model tested against the data was defined by a value of β_{dust} and T_{dust} and the normalization was linearly fit to the data. For NIKA, color corrections are expected to be negligible with respect to the calibration and statistical uncertainties ($\sim 1 - 2\%$). In the case of Herschel, we apply the color corrections given in

Table 4. Offset with respect to the X-ray center, and flux extrapolated to the NIKA channels for the 17 sub-millimeter sources identified in the 4×4 arcmin² field around MACS J1423.8+2404, obtained from the SED model described in Sect. 3.2. Despite the large uncertainties, these values allow to us estimate the impact of the contaminating sources on the reconstructed cluster properties.

Source	R.A. offset [arcsec]	Dec. offset [arcsec]	1.15 mm / 260 GHz [mJy]	2.05 mm / 150 GHz [mJy]
SMG01	-61.8	24.9	1.52 ± 0.64	0.30 ± 0.19
SMG02	-5.0	-20.0	2.39 ± 1.10	0.62 ± 0.42
SMG03	-78.1	85.1	1.51 ± 0.79	0.35 ± 0.26
SMG04	73.7	-1.2	1.05 ± 0.67	0.25 ± 0.21
SMG05	3.0	8.7	2.01 ± 0.97	0.50 ± 0.34
SMG06	-75.5	-51.5	1.13 ± 1.12	0.31 ± 0.39
SMG07	37.8	68.9	0.60 ± 0.57	0.15 ± 0.17
SMG08	-18.6	-113.9	2.53 ± 1.17	0.60 ± 0.40
SMG09	62.1	-109.8	2.15 ± 1.51	0.55 ± 0.47
SMG10	44.5	-81.6	3.79 ± 1.56	0.97 ± 0.55
SMG11	-86.8	52.2	0.09 ± 0.12	0.02 ± 0.03
SMG12	60.1	-49.4	0.05 ± 0.07	0.01 ± 0.02
SMG13	-31.9	97.4	0.05 ± 0.06	0.01 ± 0.01
SMG14	6.1	69.6	0.14 ± 0.23	0.03 ± 0.06
SMG15	93.8	28.7	0.13 ± 0.28	0.03 ± 0.07
SMG16*	-80.6	-27.4	0.08 ± 0.11	0.02 ± 0.03
SMG17*	-53.6	68.8	0.03 ± 0.04	0.01 ± 0.01

Notes. * Sources for which the position is estimated based on the 100 μ m PACS channel.

Poglitsch et al. (2010) for PACS and those available in the online documentation for SPIRE³. These coefficients were interpolated for each model using the values of β_{dust} and T_{dust} , and provide a small correction to the Herschel fluxes ($\sim 5 - 10\%$). We finally obtained a set of models distributed with respect to the posterior likelihood. Each of the model SED spectra was integrated within the NIKA bandpasses, with the distribution of fluxes giving the expected value and uncertainty. The results are summarized in Table 4.

3.3. Surface brightness profile

Figure 2 shows the flux density profiles at 150 and 260 GHz, obtained by averaging the signal from the NIKA maps in Fig. 1 in radial bins around the X-ray center. Uncertainties were computed by using the noise realizations described in Sect. 2.3: the flux density profile was computed for each noise realization and the standard deviation of all the realizations per radial bin provided the associated error bars. This allows us to account for pixel–pixel noise correlation. We also computed the profile expected from the point sources for each NIKA band by simulating the corresponding maps using the point source fluxes and positions given in Tables 2 and 4. The profile was then calculated as for the NIKA maps and the error given by the dispersion of Monte Carlo realizations of the point source maps by randomly varying their fluxes within the Gaussian errors.

³ http://herschel.esac.esa.int/Docs/SPIRE/html/spire_om.html#x1-830005.2.6

The 150 GHz profile decreases smoothly towards the center, due to the tSZ signal, except in the inner 15 arcsec, where it rises. This is consistent with the positive signal expected from the presence of radio and sub-millimeter emission from point-like sources in the cluster core. Outside the core, the cluster is detected, at the profile level, up to 60 arcsec radius.

The sub-millimeter sources shown in Fig. 4 are located in two distinct regions. Two of them are within 30 arcsec from the X-ray peak, where we expect the tSZ contribution to be the strongest, while the others are concentrated in a ring of 70 arcsec inner radius and 130 arcsec outer radius. No source is seen around 50 arcsec from the cluster center. This source distribution is reproduced, despite the large uncertainties, in the 260 GHz profile. There is an excess near the center which we attribute to the sum of tSZ and sub-millimeter sources (one of which is detected with NIKA at the map level). A dip can be seen around 1 arcmin, and another excess is seen around 100 arcsec from the center, both due to the distribution of Herschel point sources. Overall, the NIKA 260 GHz profile is consistent with that expected from the observed point source distribution.

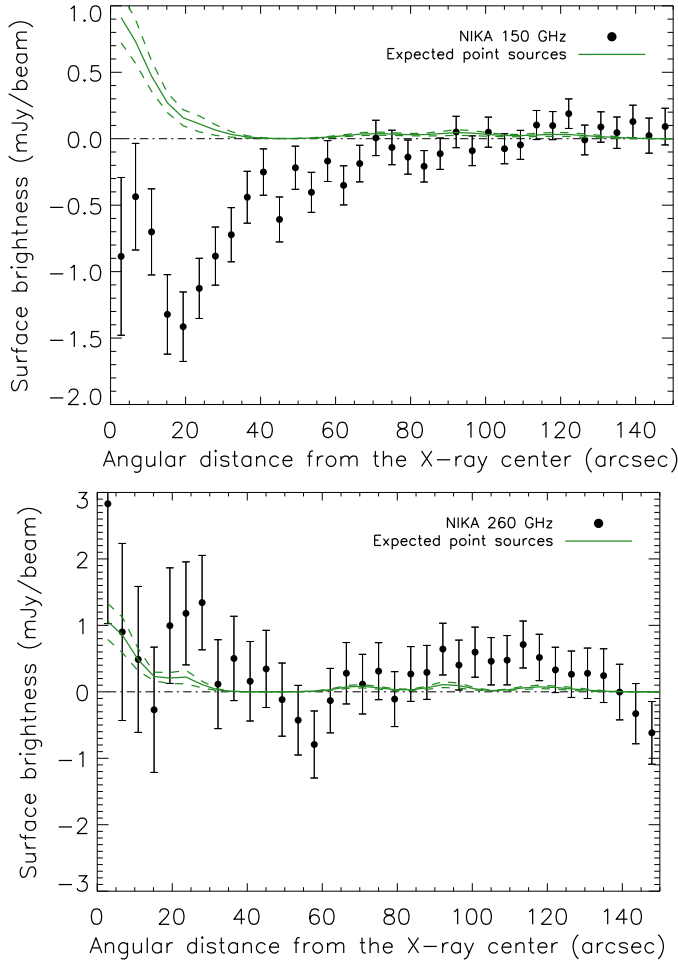


Figure 2. Profiles at 150 GHz (left) and 260 GHz (right), in units of surface brightness, of the raw map (black dots) and the contribution expected from radio and sub-millimeter point sources (green solid line). The green dashed envelope gives the 68% confidence interval on the point source profile.

4. XMM-Newton and Chandra X-ray data reduction

X-ray observations of galaxy clusters are sensitive to both the electronic density and the temperature of the ICM. The X-ray surface brightness is expressed as

$$S_X = \frac{1}{4\pi(1+z)^4} \int n_e^2 \Lambda(T_e, Z) dl, \quad (3)$$

where $\Lambda(T_e, Z)$ is the cooling function, which depends on the temperature and the ICM metallicity Z , and is roughly proportional to $T_e^{1/2}$. While X-ray imaging is mainly sensitive to the electronic density, the gas temperature can be estimated from X-ray spectroscopy. See for example [Böhringer & Werner \(2010\)](#) for a review.

4.1. Data preparation

MACS J1423.8+2404 was observed by the Chandra Advanced CCD Imaging Spectrometer (ACIS) for 115 ks (obs-ID 4195) and by the XMM-Newton European Photon Imaging Camera (EPIC) for 109 ks in total (obs-IDs 720700301 and 720700401). XMM-Newton datasets were processed by applying the latest calibration files, using the Science Analysis System (SAS) version 14.0.0 and the calibration files available in May 2015. Chandra datasets were processed using the Chandra Interactive Analysis of Observation (CIAO) software suite version 4.7 and calibration database version 4.6.5. To reduce contamination from the stationary flux of high energetic particles we applied the Very Faint mode⁴ filtering to the Chandra datasets. For XMM-Newton, we rejected events for which the keyword `PATTERN` is > 4 (for MOS1, 2) and > 13 (for PN).

The Chandra and XMM-Newton datasets were analyzed using the same technique, so unless otherwise stated, the procedures described in the following were applied to both datasets. To remove solar soft proton flare contamination we followed the procedures described in [Pratt et al. \(2007\)](#) and in the Chandra cookbook⁵ for the XMM-Newton and Chandra datasets, respectively, rejecting time intervals where the count rate exceeded 3σ with respect to the mean value. We found no flare contamination in the Chandra dataset, thus the full 115 ks observation was used; for the XMM-Newton dataset, the useful exposure time was 122 ks for MOS1+MOS2 and 41 ks for PN. To identify point sources we ran a wavelet detection algorithm with a threshold of 5σ on exposure corrected images in the $[0.7 - 7]$ keV and $[0.3 - 2]$ keV bands Chandra and XMM-Newton, respectively. The resulting source lists were merged, inspected by eye and used as a mask to remove point source contributions from the analysis.

4.2. Vignetting correction

To correct for vignetting, we followed the procedure described in [Arnaud et al. \(2001\)](#), computing a weight for each photon, defined as the ratio of the effective area at the aimpoint to that at the photon position. Using these quantities, we can perform imaging and spectroscopic analysis as if the detector had a flat response equal to that at the aimpoint. For XMM-Newton, the weights were computed using the `evigweight` routine; for Chandra we used the procedure described in [Bartalucci et al. \(in prep.\)](#). For each photon we also computed the effective exposure time, producing exposure maps that take into account bad pixels and columns. The response files for weights and spectroscopic

⁴ http://cxc.cfa.harvard.edu/cal/Acis/Cal_prods/vfbkgnd/

⁵ <http://cxc.harvard.edu/contrib/maxim/acisbg/COOKBOOK>

Please give a shorter version with: \authorrunning and/or \titilerunning prior to \maketitle
analysis were computed using the appropriate tools in CIAO (mkarf and mkacisrmf) and SAS (arfgen and rmfgen).

4.3. Background subtraction

The X-ray background is due to diffuse sky emission and an instrumental component caused by the interaction of high energetic particles with telescope instruments. To estimate the latter, we used datasets tailored to isolate this component, namely CLOSED and STOWED⁵ for XMM-Newton and Chandra, respectively. To match the observation, these datasets were skycasted and normalized in the [10–12], [12–14] keV and in the [9.5–10.6] keV band for MOS1, 2-PN and ACIS, respectively. For Chandra we used background datasets from period D, since the observation was performed in 2003. We computed the weights for the instrumental background datasets by applying the same point source masking and filtering procedures as for the observation datasets. We then subtracted from the surface brightness and temperature profiles the instrumental background evaluated using these datasets.

The residual background component is composed of thermal Galactic emission (Snowden et al. 1995) and the blending of unresolved distant point sources, known as the cosmic X-ray background (Giacconi et al. 2001). For the surface brightness profile analysis we determine a region free from cluster emission and subtract the residual mean background count rate. For the spectroscopic analysis we extracted the spectrum from the source-free region and fitted it with a multi-component model composed of two absorbed MEKAL thermal components and an absorbed power law (for details on the model used, see Pratt et al. 2009). When performing further spectroscopic analysis we added the background model as a fixed component, with an amplitude scaled by the ratio of the area of the region of interest to that of the source-free background area. The X-ray spectra were extracted and analysed in the [0.3 – 10] keV and [0.7 – 10] keV bands for XMM-Newton and Chandra, respectively.

5. Multi-wavelength comparison

Fig. 3 presents a multi-wavelength overview of MACS J1423.8+2404, including the FIRST survey (Faint Images of the Radio Sky at Twenty-Centimeters, Becker et al. 1995) observations at 1.4 GHz that provided the radio point source locations. The two radio sources discussed in Sect. 3.2 are clearly visible on the map. The complementarity of the Herschel and NIKA instruments is clear, the NIKA bands complementing the Herschel spectral coverage at lower frequencies. In addition, the angular resolution of the NIKA bands is comparable to that of SPIRE at 250 μm and PACS at 160 μm , allowing us to break the confusion in the low frequency SPIRE bands in the crowded cluster environment. The HST (Hubble Space Telescope) data from the CLASH program (Postman et al. 2012, Cluster Lensing And Supernova survey with Hubble) show the galaxy distribution. The (smoothed) Chandra X-ray image traces the gas electronic density and will be used further in Sect. 6.

Fig. 4 shows a composite multi-wavelength image of the cluster. The figure includes the NIKA 150 GHz tSZ map, the Chandra X-ray photon counts, the NIKA and Herschel sub-millimeter galaxy locations, the NVSS radio source locations, and the HST image from CLASH. We also provide, for visual comparison, the surface mass distribution model of MACS J1423.8+2404 pro-

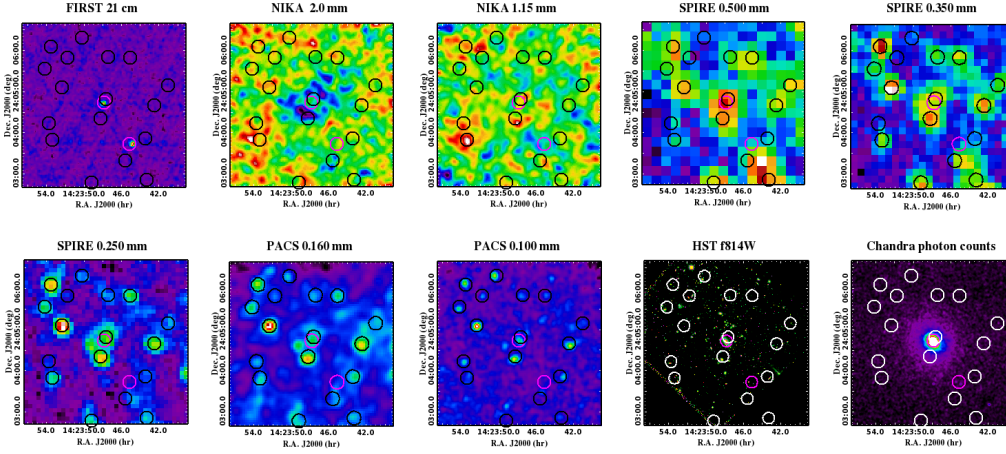


Figure 3. Multi-wavelength dataset of MACS J1423.8+2404. The origin of the data is given on top of each map. The maps have been smoothed and their range adapted for visualization purposes. The 10 arcsec radius circles show the point source locations, in black/white for sub-millimeter sources (table 3) and magenta for radio sources (table 1).

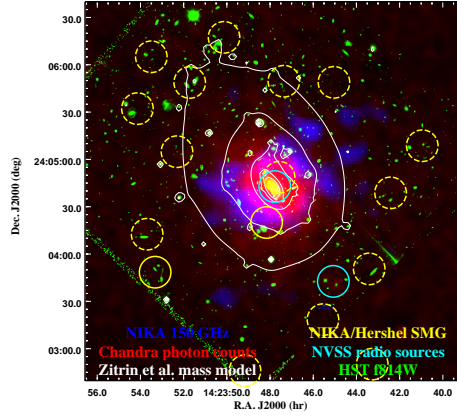


Figure 4. Composite multi-wavelength overview image of MACS J1423.8+2404. **Blue image:** NIKA 150 GHz map showing the tSZ signal. **Red image:** Chandra photon counts (Obs-ID 04195) tracing the electronic density. **White contours:** surface mass distribution model obtained by Zitrin et al. (2011) on a linear scale. **Yellow circles:** (sub-)millimeter sources candidate locations obtained using the NIKA 260 GHz map (solid line) and identified using Herschel (dashed-line). **Cyan circle:** location of the radio point sources present in the field as obtained from VLA (LaRoque et al. 2003). **Green image:** Hubble Space Telescope image using the F814W filter obtained by the CLASH program (Postman et al. 2012) showing the location of the galaxies.

duced by Zitrin et al. (2011) with the CLASH data. The image provides a detailed picture of the cluster complements the discussion of Sect. 1. The NIKA 150 GHz tSZ signal surrounds the cluster core. The hole seen in the tSZ signal is coincident with the BCG and results from the cancelling of the tSZ by the radio and sub-millimeter signal, as discussed in Sect. 3. The X-ray morphology is very peaked and the maximum of the emission coincides with the BCG. The ellipticity of the spatial mass distribution is very clear from the strong lensing map. It is also visible in the X-ray map but is less significant. It is not visible in the tSZ map due to the limited signal to noise and to the point source contamination. The galaxy distribution does not show any particular group that would be the sign of a merging event.

6. Radial thermodynamical reconstruction

The radial physical properties of the ICM were reconstructed using two approaches. The first, detailed in Sect. 6.1, uses the X-ray data only. The electronic density and the gas temperature are directly measured and serve to reconstruct all the other quantities. This approach strongly depends on the spectroscopic temperature reconstruction. The second approach, detailed in Sect. 6.2, consists of fitting jointly the tSZ data and the de-projected electronic density extracted from the X-ray data. The primary quantities are therefore the pressure and the electronic density, and as such the method depends only weakly on X-ray spectroscopy, through the electronic density reconstruction. The comparison of the two approaches is given in Sect. 6.3.

6.1. X-ray radial thermodynamic profiles

To compute the X-ray electronic pressure and entropy profiles we need to determine the temperature and electronic density profiles. The latter was computed by applying the regularized deconvolution and deprojection technique described in Croston et al. (2006). We extracted the surface brightness profile from concentric annuli centered on the X-ray peak, (R.A., Dec.) = (14:23:47.9, +24:04:42.3), in the [0.3–2.5] keV and [0.7–2.5] keV bands from the 3 combined EPIC and ACIS cameras, respectively. After background subtraction, the profiles were re-binned by a logarithmic binning factor of 1.05 to have a 3σ significance for each bin, and were point spread function (PSF) de-convolved using the analytical model of Ghizzardi (2001) for XMM-Newton. For Chandra, we assumed that the PSF is negligible with respect to the width of the bins.

The deconvolved, deprojected surface brightness profiles were converted to density using a conversion factor determined from the projected temperature profile. The latter was determined by extracting spectra from concentric annuli centered on the X-ray peak, the width of each annulus being defined to have a signal to noise ratio of 30 after background subtraction. We measured the temperature in each bin by fitting the spectrum with an absorbed MEKAL model, where the absorption was fixed to $N_H = 2.2 \times 10^{20} \text{ cm}^{-2}$ (Kalberla et al. 2005), the redshift to $z = 0.545$, adding the scaled sky background component discussed above. To interpolate the temperature profile for each surface brightness bin, we fit with the parametric model described in Vikhlinin et al. (2006). We note that the temperature correction is only a second order effect as the surface brightness is mainly dominated by the electronic density (see equation 3). The differences in temperature reconstruction between Chandra and XMM-Newton (e.g., Schellenberger et al. 2015) thus do not affect the electronic density. To de-project the temperature profile, we measured the spectroscopic-like temperature (Mazzotta et al. 2004) using the weighting scheme implemented in Vikhlinin (2006), where the observed temperature profile is modeled as the weighted sum of concentric plasma shells each at a different temperature. As for the density profiles, we take into account the PSF effects for XMM-Newton.

Finally, M_{500} , the cluster mass enclosed within R_{500} ⁶, was calculated by iteration about the $M_{500}-Y_X$ relation of Arnaud et al. (2010).

⁶ R_{500} is the radius within which the mean cluster density is equal to 500 times the critical density of the Universe at the cluster’s redshift.

6.2. Modeling of the ICM and joint tSZ/X-ray fitting procedure

To fit the tSZ and electronic density jointly, we modeled the ICM using the approach described in detail in Adam et al. (2015). As seen in Sect. 5 and as emphasized by Morandi et al. (2010), MACS J1423.8+2404 is elliptical. Nevertheless, we assume spherical symmetry because this work does not focus on its geometry, but on the impact of the presence of point sources on the pressure profile reconstruction. Moreover, the significance of the NIKA 150 GHz tSZ map is not sufficient to constrain any asymmetry.

The radial distribution of the cluster electronic pressure was modeled by a gNFW profile (Nagai et al. 2007), described by

$$P_e(r) = \frac{P_0}{\left(\frac{r}{r_p}\right)^c \left(1 + \left(\frac{r}{r_p}\right)^a\right)^{\frac{b-c}{a}}}. \quad (4)$$

The parameter P_0 is a normalization constant; r_p is a characteristic radius; and a , b , and c set the slopes at intermediate, large, and small radii, respectively. This model was chosen to allow the description of the profile at all scales. The electronic density was modeled by a *Simplified Vikhlinin Model* (Vikhlinin et al. 2006),

$$n_e(r) = n_{e0} \left[1 + \left(\frac{r}{r_c}\right)^2\right]^{-3\beta/2} \left[1 + \left(\frac{r}{r_s}\right)^\gamma\right]^{-\epsilon/2\gamma}. \quad (5)$$

The parameter n_{e0} is the central density, r_c is the core radius and β is related to the slope of the profile. The second term allows a of the steepening of the profile at large scales. The parameter ϵ gives the change in the slope, r_s the radius at which the transition occurs, and γ the width of the transition. In the following, we set $\gamma = 3$ since this value provides a good fit to all clusters considered in the analysis of Vikhlinin et al. (2006).

With the pressure and the density in hand, we compute the temperature profile assuming the ideal gas law, $k_B T_e(r) = \frac{P_e(r)}{n_e(r)}$, and the entropy profile as $K(r) = \frac{P_e(r)}{n_e(r)^{5/3}}$. The total mass, assuming hydrostatic equilibrium, enclosed within r is then given by

$$M_{\text{HSE}}(r) = -\frac{r^2}{\mu_{\text{gas}} m_p n_e(r) G} \frac{dP_e(r)}{dr} \quad (6)$$

where m_p is the proton mass, G is Newtons constant, and $\mu_{\text{gas}} = 0.61$ the mean molecular weight of the gas.

The parameter space was sampled using the Markov Chain Monte Carlo (MCMC) approach detailed in Adam et al. (2015), jointly fitting the 150 GHz NIKA tSZ map and the electronic density profile computed from the X-ray data. We added an additional constraint on the total tSZ flux of the cluster using the Planck Compton parameter map (Planck Collaboration et al. 2015b). The tSZ models were convolved with the effective transfer function of the observations, including the beam smoothing and the large scale filtering cutoff due to the removal of the atmospheric noise. MACS J1423.8+2404 is not present in the Planck catalogue of tSZ sources (Planck Collaboration et al. 2015a), but we obtained an upper limit on its flux by integrating the Compton parameter map (Planck Collaboration et al. 2015b) using aperture photometry. The error on the flux was computed by performing the same measurement randomly around the cluster, where the noise is homogeneous. The flux was measured to be $Y_{\text{tot}}^{\text{Planck}} = (0.40 \pm 0.66) \times 10^{-3} \text{ arcmin}^2$. The MCMC sampling procedure also marginalizes over nuisance parameters such as the zero level of the NIKA

Please give a shorter version with: \authorrunning and/or \titilerunning prior to \maketitle

map, the calibration uncertainty, and the central point source flux and position when included in the fit. Full details can be found in [Adam et al. \(2015\)](#).

The constraints obtained on the pressure and electronic density profiles are almost independent. However, each model compared to the data includes relativistic corrections computed using the radial temperature profile, given by the ratio of the electronic pressure and density profiles, for each radial shell of the ICM. This affects essentially the constraint on the pressure profile but the effect is very small compared to the uncertainties. Therefore, the constraint on the electronic density profile is driven by the X-ray data and that on the pressure is largely driven by the tSZ data. The Planck constraint on the overall tSZ flux is relatively weak due to the location of the cluster on the sky and the noise inhomogeneity. However, Planck provides an upper limit that allows the MCMC procedure to avoid models which diverge at large scales, where NIKA is not sensitive. Planck and NIKA are therefore highly complementary to constrain the pressure profile from small to large scales.

6.3. Results

MACS J1423.8+2404 is known to be a typical cool core (e.g. [Morandi et al. 2010](#)), so we used the pressure profile parameters found for such clusters by [Arnaud et al. \(2010\)](#) as a baseline: $(a, b, c) = (1.2223, 5.4905, 0.7736)$. The X-ray photon count provided by XMM-Newton is larger than that of Chandra, allowing us to probe the cluster ICM up to larger radii. We therefore used the XMM-Newton results as a reference and we cross-checked our results with the Chandra data.

6.3.1. Impact of the point sources at millimeter wavelengths

The impact of the point source contamination on the reconstructed pressure profile was tested by considering three different cases:

1. The presence of point sources was ignored and we fit the parameters P_0 and r_p , keeping the slope parameters fixed to their baseline values. This case is referred as model 1 (M1).
2. The point sources were subtracted assuming the fluxes of Table 4 and we repeated the fit of model M1. This case is referred as model 2 (M2).
3. The point sources were subtracted assuming the fluxes given in Table 4, but possible residuals of the central sources were also fitted. In this case, we also released the constraint on the inner and outer slope parameters, c and b , which are also fitted. The intermediate slope parameter a was held fixed because it is strongly degenerate with the characteristic radius r_p and the outer slope b . This case is referred as model 3 (M3).

Comparison of the output pressure profile from models M1 and M2 (see Fig. 5) allows a direct estimation of the impact of point sources. The use of model M3 was motivated by the large uncertainties on the point source fluxes as shown in Table 4. As discussed in Sect. 3.3 and shown on Fig. 2, the sources that are in the outer region of the cluster do not contribute significantly to the radial flux density. However, this is not the case for the central sources, in particular for RS1 and SMG05. We expect a significant correlation between the flux of these sources and the pressure profile parameters related to the cluster core, such as P_0 , r_p and c . Those related to the external regions of the profile are also affected, due to projection effects. Thus model M3 allows us to test

Please give a shorter version with: \authorrunning and/or \titilerunning prior to \maketitle

the constraints that can be obtained on the pressure profile in the cluster core in the presence of a contaminating central point source, when no strong prior on its flux is available, as is the case here.

Figure 5 shows the resulting pressure profiles. Model M1 is lower than the two others at all scales except above 1000 kpc, where NIKA does not provide a direct constraint due to the large scale filtering. This corresponds to the fact that point sources, and in particular those close to the core, compensate the overall flux amplitude of the cluster. Apart from its normalization, the shape of the pressure profile is similar for M1 and M2 as the constraint on r_p is not significantly affected by the point source subtraction. The effect of the source in the cluster core is then diluted over the entire profile via the $P_0 - r_p$ degeneracy. The results for M3 are close to those for M2 but the error contours are larger because of the extra freedom available in the parameter space. This is particularly true in the inner region, where the error on the flux of the fitted point source propagates into the profile via the parameter degeneracies. The inner pressure distribution thus remains poorly constrained unless the point source is subtracted with sufficient accuracy. At large scales, around 800 kpc, M3 is slightly above M2. However, the differences observed between models are not significant with respect to the uncertainties, which are dominated by the low exposure time spent with NIKA on this cluster.

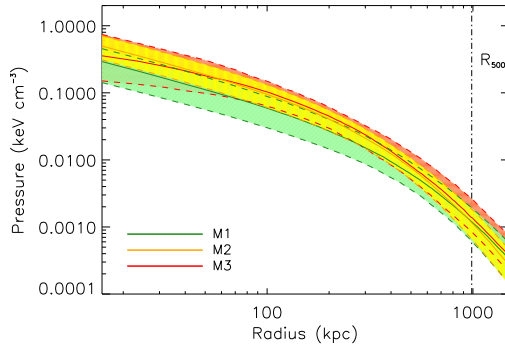


Figure 5. Constraint on the pressure profile of MACS J1423.8+2404 for the three models M1 (green), M2 (orange) and M3 (red). The solid lines gives the central profiles and the dashed line represent the 68% confidence limits.

To search for possible deviations from a spherical relaxed morphology, we subtracted the best-fit model of M3 from the NIKA 150 GHz map. Fig. 6 shows the resulting raw, point source subtracted, tSZ best-fit, and residual 150 GHz maps. After removing the point sources (fluxes in Table 4) and the best-fit of model M3, the cluster appears to be fairly compact. The small excess towards the south has a significance of less than 2σ and can be attributed to a poor subtraction of SMG05, whose position is very close on the map. The signal is overall relatively spherical, as confirmed by the residual map, which is consistent with the noise. Deeper tSZ observations would be necessary in order to further constrain the morphology of the cluster, in particular in terms of ellipticity.

6.3.2. Comparison between tSZ and X-ray derived cluster thermodynamics

Fig. 7 shows a comparison of the MCMC constraints and the data used to obtain them. The left panel presents the best-fit and the uncertainties of model M3 compared to the projected flux density profile from the point source-subtracted NIKA data. The data points are correlated across the profile

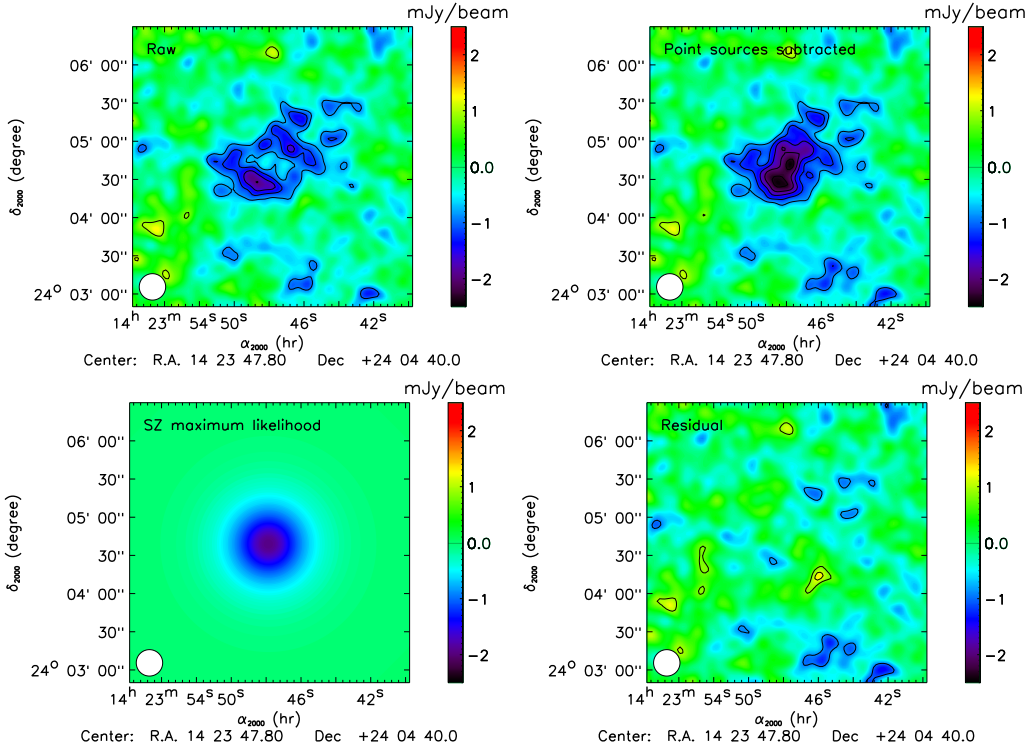


Figure 6. Comparison of the raw 150 GHz input NIKA map (top left), the same map after point source subtraction (top right), the best-fit tSZ model (bottom left), and the final residual map. Contours are the same as in Fig. 1 and give the significance in unit of σ , starting from $\pm 2 \sigma$.

and we accounted for this in the MCMC analysis. The model uncertainties increase significantly in the cluster core because the flux estimate (and associated uncertainty) of the central point source is included in the fit. The model is greater than zero at large scales because the zero level of the map (one of the nuisance parameters included in the fit) is slightly positive. The right panel shows the best-fit to the XMM-Newton electronic density and its 68% confidence limit. We also show the Chandra data for comparison. The X-ray data are well described by the SVM model, except at radii smaller than 30 kpc, where we observe a flattening of the data with respect to the model. However, this region is not probed directly by NIKA and this deviation is not significant in the context of the joint tSZ/X-ray analysis.

The top left panel of Fig. 8 shows the deprojected pressure profile of MACS J1423.8+2404 as derived from our MCMC analysis of NIKA data, and from X-ray measurements only. While deep X-ray observations can only infer the pressure (using the product of the de-projected density and temperature profiles), the tSZ effect directly measures it. The comparison of the two, which are completely independent, is therefore an important cross check for both constraints. The data points represent measurements obtained from XMM-Newton and Chandra, and the shaded area is the 68% confidence limit given by model M2. The upper and lower dashed lines give respectively the upper and lower limits from all the tSZ based models M1, M2 and M3. The Chandra constraint is slightly more peaked than that from XMM-Newton. In turn, the latter is slightly more peaked than that from NIKA, but all profiles are compatible within error bars. These results confirm that the point spread function deconvolution of the XMM-Newton data performs well and that the model extrapolation of the tSZ data accurately describes the pressure profile at the cluster center. At large

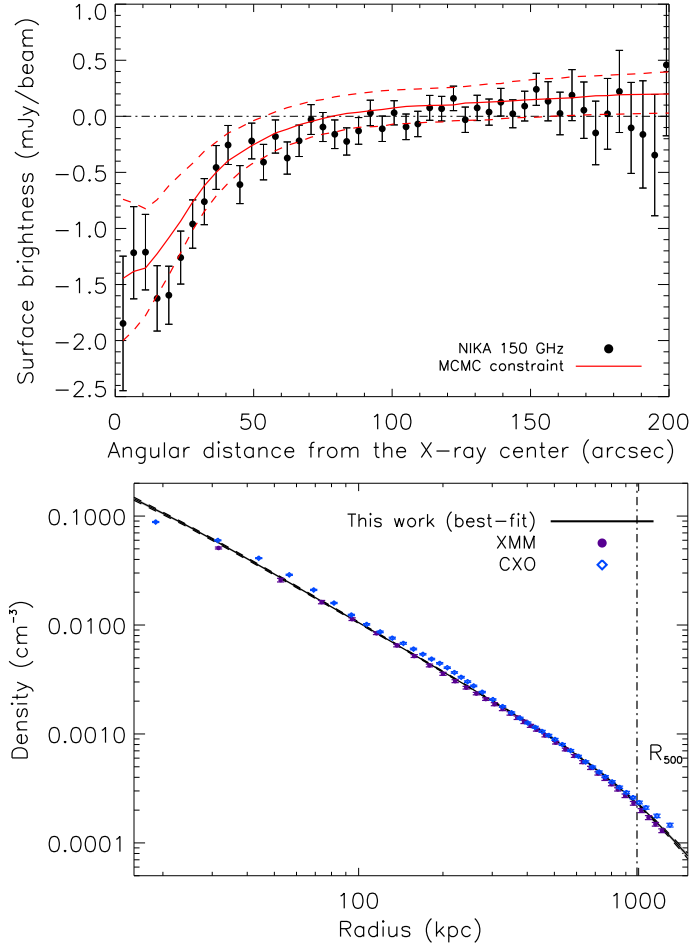


Figure 7. MCMC best-fit and constraints compared to the NIKA tSZ and XMM-Newton X-ray data used to obtain them. **Left:** projected tSZ flux density profile from the point source subtracted NIKA data (black dots) and for the best-fit M3 model (red solid line). Uncertainties at 68% confidence limits are given by the red dashed lines. We note that, in practice, it is the tSZ map which is compared to the models and not the profile. **Right:** deprojected electronic density profile obtained from XMM-Newton (purple dots) and Chandra (CXO for Chandra X-ray Observatory, blue diamonds). The MCMC best-fit model is given by the black line, and its uncertainties at 68% confidence limits are shown by the black dashed lines. The characteristic radius measured from XMM-Newton data, $R_{500} = 986 \pm 10$ kpc, is represented as a vertical dashed line.

radii, the Chandra measurement is not available due to a lower photon count rate than XMM-Newton, making the two observations highly complementary. The tSZ pressure profile decreases slightly more slowly than that from XMM-Newton, but the effect is not significant with respect to the uncertainties.

We compared our measurements to the universal pressure profile obtained by [Arnaud et al. \(2010\)](#) using REXCESS ([Böhlinger et al. 2007](#)), a representative sample of nearby clusters. The green and orange solid lines show the mean profiles for the cool core and morphologically disturbed sub-samples used by [Arnaud et al. \(2010\)](#), respectively. The normalization (eqn. 13 of [Arnaud et al. \(2010\)](#)) was accounted for using the XMM-Newton mass measurement of MACS J1423.8+2404, and neglecting the mass dependance of the shape of the profile. The observed pressure distribution of MACS J1423.8+2404 compares well to the mean cool core profile both in shape and amplitude. The mean morphologically disturbed profile is consistent with the observations at large scales,

Please give a shorter version with: \authorrunning and/or \titilerunning prior to \maketitle

but deviates significantly in the core, being much shallower than the observations because of the redistribution of the thermal energy from merging events in such clusters. The relaxed dynamical state of MACS J1423.8+2404 is therefore confirmed by its pressure profile. We stress that the point source subtraction is crucial to this result (cf., model M1).

Finally, we note that our measurement is fully compatible with the tSZ interferometric results obtained by Bonamente et al. (2012) on the same cluster, but with a significant improvement of the uncertainty.

The constraints on temperature and entropy, directly related to those from the pressure and the density (see Sect. 6.2), are also given in Fig. 8. The red contours use the tSZ derived pressure and the XMM-Newton derived density, while the data points are X-ray only measurements based on spectroscopic data. Since both the temperature and the entropy are proportional to the pressure, this figure reproduces the comparison of the top left panel of Fig. 8, but focussing on different thermodynamic quantities. The temperature profile is typical of a cool core cluster, with a core temperature of about 4 keV, reaching about 10 keV at a radial distance of 200 kpc. The de-projected XMM-Newton and Chandra temperature profiles are in good agreement over the full radial range. The shapes of the two profiles are also consistent, showing a peak of the temperature at the same radius, even though the Chandra profile is somewhat lower ~ 1 keV, contrary to what is generally found (e.g. Mahdavi et al. 2013 or Martino et al. 2014).

The spatial distribution of entropy is an important tool for investigating cluster formation as it is related to the structure of the ICM and records the thermodynamical history of the gas (see Voit 2005, for a review). Numerical simulations including gravitational processes only were used by Voit et al. (2005) to obtain a baseline entropy profile that is well described by a simple power law of the form $K(r) = 1.32K_{200} (r/R_{200})^{1.1}$. Pratt et al. (2010) used the REXCESS sample to investigate the properties of entropy in a representative sample of nearby clusters, observing a central excess in dynamically disturbed systems and a power law profile in cool core systems (see also results obtained by Cavagnolo et al. (2009) using the ACCEPT data). The entropy can be described by a power law plus constant, $K(r) = K_0 + K_{100} (r/100 h_{70}^{-1} \text{ kpc})^{\alpha_K}$. Disturbed systems present a higher plateau (up to almost two orders of magnitude) and a shallower slope than cool cores. We used the best-fit (power law plus constant) profiles of REXCESS clusters (see Tab. 3 of Pratt et al. 2010) to derive the median entropy profile of cool core and morphologically disturbed clusters, which we compare to our data in the bottom-left panel of Fig. 8. The baseline profile of Voit et al. (2005) is also included using the normalization described in Pratt et al. (2010) appropriate for the mass of MACS J1423.8+2404. The observed entropy profile compares very well with the median cool core profile from the REXCESS sample; it is almost consistent with the single power law self-similar expectation from non-radiative simulations (Voit et al. 2005). For comparison, the median morphologically disturbed median profile is about one order of magnitude higher than our data at the cluster core. At large scales, both XMM-Newton and the tSZ derived constraints indicate a flattening of the profile, but it is not significant compared to the error bars. As for the pressure profile, the entropy distribution clearly shows that MACS J1423.8+2404 behaves as a typical cool core, and that it is indeed a relaxed system (as discussed in Sect. 1, e.g. Kartaltepe et al. 2008; Limousin et al. 2010).

We can derive the mass profile assuming hydrostatic equilibrium, as described in Sect. 6.2. The bottom right panel of Fig. 8 compares the constraints obtained when combining the X-ray and tSZ

Please give a shorter version with: \authorrunning and/or \titilerunning prior to \maketitle

data with those obtained using X-ray data only. The constraints are fully compatible at all scales within the 68% confidence limit. We obtained $R_{500} = 1123^{+328}_{-187}$ kpc, which gives $M_{500} = 6.9^{+6.5}_{-2.9} \times 10^{14} M_{\odot}$, in the case of model M3. These results are fully consistent with those obtained from XMM-Newton data only: ($R_{500} = 986 \pm 10$ kpc and $M_{500} = 4.9 \pm 0.15 \times 10^{14} M_{\odot}$), but with larger uncertainties. The total integrated Compton parameter was constrained to be $Y_{\text{tot}} = 0.85^{+0.61}_{-0.30} \times 10^{-3}$ arcmin², in agreement with, but slightly larger than the Planck value from aperture photometry. We summarize the main recovered properties of MACS J1423.8+2404 in Table 5.

Table 5. Summary of the recovered properties of MACS J1423.8+2404.

$M_{500,X \text{ only}}$	$4.9 \pm 0.15 \times 10^{14} M_{\odot}$
$M_{500,X/tSZ}$	$6.9^{+6.5}_{-2.9} \times 10^{14} M_{\odot}$
$R_{500,X \text{ only}}$	986 ± 10 kpc
$R_{500,X/tSZ}$	1123^{+328}_{-187} kpc
$\theta_{500,X \text{ only}}$	2.50 ± 0.03 arcmin
$\theta_{500,X/tSZ}$	$2.85^{+0.83}_{-0.47}$ arcmin
Y_{tot}	$0.85^{+0.61}_{-0.30} \times 10^{-3}$ arcmin ²

The X-ray results present error bars smaller than those derived from NIKA+Planck tSZ data. Nevertheless, we emphasize that both X-ray datasets are particularly exceptional for this cluster (about 30 hours of exposure time for both instruments), while the tSZ ones have been obtained with only 1.47 hours on target. Even in this situation, NIKA already provides essential information that allows the reconstruction of the thermodynamical structure of the cluster to reasonable accuracy, especially when combined with X-ray electronic density.

7. Conclusions and perspectives

7.1. Conclusions

The cluster of galaxies MACS J1423.8+2404 was observed at 150 and 260 GHz using the NIKA camera at the IRAM 30-meter telescope. The target was detected at 150 GHz in only 1.47 hours and the data show evidence for the presence of a contaminating central point source, as expected from previous radio observations. The 260 GHz NIKA band allows the further identification of two sub-millimeter contaminant galaxies.

The NIKA observations were combined with external datasets taken in multiple wavelengths to investigate the cluster morphology and the dynamical state of the gas. The object MACS J1423.8+2404 is a typical cool core, which appears to be relaxed and elliptical. A total of 17 sub-millimeter sources were identified in the NIKA field using Herschel data, and two radio sources were known from external radio observations.

The fluxes of the two radio sources were extrapolated to the NIKA bands by fitting a power law SED to external photometric measurements. The sub-millimeter sources were extrapolated to the NIKA bands by modeling their SED with a grey-body spectrum and by jointly fitting the Herschel and NIKA photometric data. This work shows the excellent complementarity between the two instruments in terms of frequency coverage and angular resolution. Comparison of the flux density

Please give a shorter version with: \authorrunning and/or \titilerunning prior to \maketitle

derived directly from NIKA data shows good agreement with the expectation from extrapolated point source fluxes at the same frequencies. The contamination from point sources can, therefore, be estimated and subtracted from the tSZ map, if external data are available at complementary wavelengths.

The pressure profile of MACS J1423.8+2404 was then measured by modeling and jointly fitting the NIKA and Planck (i.e. Y_{tot}) data. We have evaluated the impact of the point source contamination on its reconstruction. We find that neglecting the sources leads to an overall underestimate of the profile, which is small compared to the error bars in the case of the available data, but which could become significant when deeper tSZ observations are available. Moreover, in the case of the presence of a point source at the cluster center with no strong priors on its flux, the inner pressure profile remains poorly constrained by the data. Consequently, the morphological characteristics of the cluster could be misunderstood in such cases. We used XMM-Newton and Chandra X-ray observations to derive the cluster thermodynamical radial distributions. The deprojected electronic density has been combined with the tSZ data, providing a measurement of the pressure, and used to infer the temperature and the entropy profiles. The X-ray only (including spectroscopy) and the tSZ+X-ray (without spectroscopy) constraints are consistent within their uncertainties, and confirm that MACS J1423.8+2404 is a relaxed cool core cluster.

7.2. Prospect for NIKA2 observations

These observations and the present analysis are part of the NIKA tSZ pilot study aiming at characterizing the potential outcomes of future NIKA2 tSZ observations.

Clusters are crowded environments, therefore, in high angular resolution tSZ observations like those of NIKA2 we expect the detection of a large number of point sources, as demonstrated in Adam et al. (2014), Adam et al. (2015) and in the present work. These sources are a contaminant in the context of tSZ studies. We have shown here that their contribution can be estimated and accounted for if external data are available. Sub-millimeter point sources should not be a problem because they can be identified at 260 GHz and marginalized over at 150 GHz. They can even be masked without removing the information on the tSZ profile. Radio point sources can be more problematic. Unless they are as strong as the tSZ signal, they can only be identified using external data. They are generally correlated with the central BCG and will prevent NIKA2 from putting any constraint on the core pressure distribution unless their SED is well measured at lower frequencies. If no external data are available, the removal of the contaminants will require the use of extra high angular resolution observations obtained with interferometers at similar frequencies, such as the IRAM NOthern Extended Millimeter Array (NOEMA)⁷.

Point sources around clusters are also interesting in themselves and the high complementarity between Herschel and NIKA could be used, for example, to search for distant lensed galaxies (see for example Egami et al. 2010) or to study star formation at high redshift. This should be an extra outcome of the NIKA2 tSZ observations.

The present work has also shown how X-ray and tSZ data can be used to constrain the temperature and the entropy profiles of galaxy clusters independently from X-ray spectroscopy, using the density and pressure profiles. Moving to high redshift, X-ray observations become time expen-

⁷ <http://iram-institute.org/EN/noema-project.php>

Please give a shorter version with: \authorrunning and/or \titilerunning prior to \maketitle

sive and high-quality X-ray mapping becomes challenging, due to the redshift dimming. In this context, the results obtained in this study show that we are able to constrain the ICM thermodynamics with a good accuracy by combining resolved NIKA tSZ observations and X-ray mapping. This will be particularly important for distant clusters observed with NIKA2, for which we will not benefit from deep X-ray observations tuned for spatially resolved X-ray spectroscopy, and where only a mean temperature can be obtained from X-ray data. In addition, X-ray constraints on the cluster thermodynamics directly depend on the energy calibration of the instrument, which can be source of discrepancy. NIKA tSZ data offer a third independent measurement, independent from X-ray spectroscopy, providing a cross check of the temperature measurement of clusters. This can help reducing the systematic effects affecting all these observations, which are essential for mass estimates when using clusters as a cosmological probe.

Acknowledgements. We thank Marco De Petris for useful comments. We would like to thank the IRAM staff for their support during the NIKA campaign. We thank Karin Dassas for helping us obtaining the Herschel data. This work has been partially funded by the Foundation Nanoscience Grenoble, the ANR under the contracts "MKIDS" and "NIKA". This work has been partially supported by the LabEx FOCUS ANR-11-LABX-0013. This work has benefited from the support of the European Research Council Advanced Grant ORISTARS under the European Union's Seventh Framework Program (Grant Agreement no. 291294). This work has benefitted from the support of the European Research Council Advanced Grant M2C under the European Unions Seventh Framework Programme (Grant Agreement no. 340519). The NIKA dilution cryostat was designed and built at the Institut Néel. In particular, we acknowledge the crucial contribution of the Cryogenics Group and, in particular Gregory Garde, Henri Rodenas, Jean Paul Leggeri, and Philippe Camus. We acknowledge the use of the IGLO-HESIOD service from the Integrated Data & Operation Center (IDOC). Support for IDOC is provided by CNRS & CNES. R. A. would like to thank the ENIGMASS French LabEx for funding this work. B. C. acknowledges support from the CNES post-doctoral fellowship program. A. R. acknowledges support from the CNES doctoral fellowship program. E. P. acknowledges the support of the French Agence Nationale de la Recherche under grant ANR-11-BD56-015.

References

- Adam, R. et al. 2015, A&A, 576, A12, 1410.2808
———. 2014, A&A, 569, A66, 1310.6237
Arnaud, M., Neumann, D. M., Aghanim, N., Gastaud, R., Majerowicz, S., & Hughes, J. P. 2001, A&A, 365, L80, astro-ph/0011198
Arnaud, M., Pratt, G. W., Piffaretti, R., Böhringer, H., Croston, J. H., & Pointecouteau, E. 2010, A&A, 517, A92, 0910.1234
Becker, R. H., White, R. L., & Helfand, D. J. 1995, ApJ, 450, 559
Birkinshaw, M. 1999, Phys. Rep., 310, 97, arXiv:astro-ph/9808050
Bleem, L. E. et al. 2014, ArXiv e-prints, 1409.0850
Böhringer, H. et al. 2007, A&A, 469, 363, astro-ph/0703553
Böhringer, H., & Werner, N. 2010, A&A Rev., 18, 127
Bonamente, M. et al. 2012, New Journal of Physics, 14, 025010, 1112.1599
Borgani, S., & Kravtsov, A. 2011, Advanced Science Letters, 4, 204, 0906.4370
Bourrion, O. et al. 2011, JINST, 6, P06012, 1102.1314
Bourrion, O., Vescovi, C., Bouly, J. L., Benoit, A., Calvo, M., Gallin-Martel, L., Macias-Perez, J. F., & Monfardini, A. 2012, Journal of Instrumentation, 7, 7014, 1204.1415
Calvo, M. et al. 2013, A&A, 551, L12
Cantalupo, C. M., Borrill, J. D., Jaffe, A. H., Kisner, T. S., & Stompor, R. 2010, ApJS, 187, 212, 0906.1775
Carlstrom, J. E., Holder, G. P., & Reese, E. D. 2002, ARA&A, 40, 643, arXiv:astro-ph/0208192
Catalano, A. et al. 2014, A&A, 569, A9, 1402.0260
Cavagnolo, K. W., Donahue, M., Voit, G. M., & Sun, M. 2009, ApJS, 182, 12, 0902.1802
Coble, K. et al. 2007, AJ, 134, 897, astro-ph/0608274
Condon, J. J., Cotton, W. D., Greisen, E. W., Yin, Q. F., Perley, R. A., Taylor, G. B., & Broderick, J. J. 1998, AJ, 115, 1693

- Croston, J. H., Arnaud, M., Pointecouteau, E., & Pratt, G. W. 2006, *A&A*, 459, 1007, astro-ph/0608700
- da Silva, A. C., Kay, S. T., Liddle, A. R., & Thomas, P. A. 2004, *MNRAS*, 348, 1401, astro-ph/0308074
- Ebeling, H., Edge, A. C., & Henry, J. P. 2001, *ApJ*, 553, 668, astro-ph/0009101
- Egami, E. et al. 2010, *A&A*, 518, L12, 1005.3820
- Ghizzardi, S. 2001, XMM-SOC-CAL-TN-0022
- Giacconi, R. et al. 2001, *ApJ*, 551, 624, astro-ph/0007240
- Griffin, M. J. et al. 2010, *A&A*, 518, L3, 1005.5123
- Guennou, L. et al. 2014, *A&A*, 561, A112, 1311.6922
- Hasselfield, M. et al. 2013, *J. Cosmology Astropart. Phys.*, 7, 8, 1301.0816
- Hlavacek-Larrondo, J., Fabian, A. C., Edge, A. C., Ebeling, H., Sanders, J. S., Hogan, M. T., & Taylor, G. B. 2012, *MNRAS*, 421, 1360, 1110.0489
- Itoh, N., Kohyama, Y., & Nozawa, S. 1998, *ApJ*, 502, 7, arXiv:astro-ph/9712289
- Kalberla, P. M. W., Burton, W. B., Hartmann, D., Arnal, E. M., Bajaja, E., Morras, R., & Pöppel, W. G. L. 2005, *A&A*, 440, 775, astro-ph/0504140
- Kartalpe, J. S., Ebeling, H., Ma, C. J., & Donovan, D. 2008, *MNRAS*, 389, 1240, 0806.4019
- Kitayama, T. 2014, *Progress of Theoretical and Experimental Physics*, 2014, 060000, 1404.0870
- Komatsu, E. et al. 2001, *PASJ*, 53, 57, astro-ph/0006293
- Korngut, P. M. et al. 2011, *ApJ*, 734, 10, 1010.5494
- LaRoque, S. J. et al. 2003, *ApJ*, 583, 559
- Limousin, M. et al. 2010, *MNRAS*, 405, 777, 0911.4125
- Mahdavi, A., Hoekstra, H., Babul, A., Bildfell, C., Jeltima, T., & Henry, J. P. 2013, *ApJ*, 767, 116, 1210.3689
- Martino, R., Mazzotta, P., Bourdin, H., Smith, G. P., Bartalucci, I., Marrone, D. P., Finoguenov, A., & Okabe, N. 2014, *MNRAS*, 443, 2342, 1406.6831
- Mazzotta, P., Rasia, E., Moscardini, L., & Tormen, G. 2004, *MNRAS*, 354, 10, astro-ph/0404425
- Monfardini, A. et al. 2014, *Journal of Low Temperature Physics*, 176, 787, 1310.1230
- . 2011, *ApJS*, 194, 24, 1102.0870
- . 2010, *A&A*, 521, A29, 1004.2209
- Morandi, A., Pedersen, K., & Limousin, M. 2010, *ApJ*, 713, 491, 0912.2648
- Motl, P. M., Hallman, E. J., Burns, J. O., & Norman, M. L. 2005, *ApJ*, 623, L63, astro-ph/0502226
- Mroczkowski, T. et al. 2015, *ArXiv e-prints*, 1501.05051
- Nagai, D. 2006, *ApJ*, 650, 538, astro-ph/0512208
- Nagai, D., Vikhlinin, A., & Kravtsov, A. V. 2007, *ApJ*, 655, 98, arXiv:astro-ph/0609247
- Planck Collaboration. 2015, *ArXiv e-prints*, 1502.01589
- Planck Collaboration et al. 2013a, *ArXiv e-prints*, 1303.5089
- . 2013b, *ArXiv e-prints*, 1303.5080
- . 2013c, *A&A*, 550, A131, 1207.4061
- . 2015a, *ArXiv e-prints*, 1502.01598
- . 2015b, *ArXiv e-prints*, 1502.01596
- Poglitsch, A. et al. 2010, *A&A*, 518, L2, 1005.1487
- Pointecouteau, E., Giard, M., Benoit, A., Désert, F. X., Aghanim, N., Coron, N., Lamarre, J. M., & Delabrouille, J. 1999, *ApJ*, 519, L115
- Ponthieu, N., Grain, J., & Lagache, G. 2011, *A&A*, 535, A90, 1111.0766
- Postman, M. et al. 2012, *ApJS*, 199, 25, 1106.3328
- Pratt, G. W. et al. 2010, *A&A*, 511, A85, 0909.3776
- Pratt, G. W., Böhringer, H., Croston, J. H., Arnaud, M., Borgani, S., Finoguenov, A., & Temple, R. F. 2007, *A&A*, 461, 71, astro-ph/0609480
- Pratt, G. W., Croston, J. H., Arnaud, M., & Böhringer, H. 2009, *A&A*, 498, 361, 0809.3784
- Rawle, T. D. et al. 2012, *ApJ*, 747, 29, 1201.1294
- Reichardt, C. L. et al. 2013, *ApJ*, 763, 127, 1203.5775
- Savage, R. S., & Oliver, S. 2007, *ApJ*, 661, 1339, astro-ph/0512597
- Sayers, J. et al. 2013a, *ApJ*, 768, 177, 1211.1632
- . 2013b, *ApJ*, 764, 152, 1209.5129

Please give a shorter version with: \authorrunning and/or \titilerunning prior to \maketitle

- Schellenberger, G., Reiprich, T. H., Lovisari, L., Nevalainen, J., & David, L. 2015, *A&A*, 575, A30, 1404.7130
- Schmidt, R. W., & Allen, S. W. 2007, *MNRAS*, 379, 209, astro-ph/0610038
- Snowden, S. L. et al. 1995, *ApJ*, 454, 643
- Sunyaev, R. A., & Zel'dovich, Y. B. 1972, *Astrophys. Space Phys. Res.*, 4, 173
- . 1980, *ARA&A*, 18, 537
- Vikhlinin, A. 2006, *ApJ*, 640, 710, astro-ph/0504098
- Vikhlinin, A., Kravtsov, A., Forman, W., Jones, C., Markevitch, M., Murray, S. S., & Van Speybroeck, L. 2006, *ApJ*, 640, 691, astro-ph/0507092
- Voit, G. M. 2005, *Reviews of Modern Physics*, 77, 207, astro-ph/0410173
- Voit, G. M., Kay, S. T., & Bryan, G. L. 2005, *MNRAS*, 364, 909, astro-ph/0511252
- Witzel, A., Pauliny-Toth, I. I. K., Nauber, U., & Schmidt, J. 1979, *AJ*, 84, 942
- Young, A. H. et al. 2014, *ArXiv e-prints*, 1411.0317
- Zitrin, A., Broadhurst, T., Barkana, R., Rephaeli, Y., & Benítez, N. 2011, *MNRAS*, 410, 1939, 1002.0521

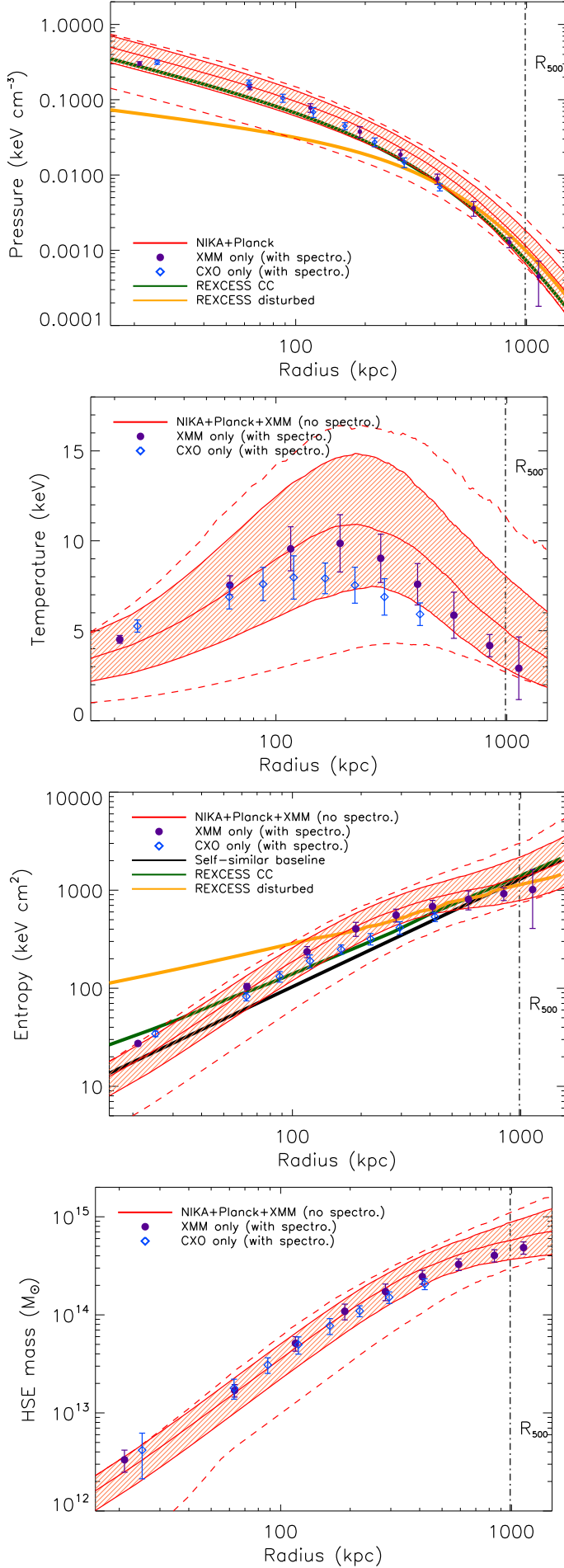


Figure 8. MCMC constraints on the deprojected radial profiles of the pressure (top left), the temperature (top right), the entropy (bottom left), and the hydrostatic mass (bottom right). The Chandra only and XMM-Newton only measurements are given by the blue diamonds and the purple dots, respectively. The red shaded area shows the MCMC 68% confidence limit from model M2, the central solid line corresponding to the best-